RESEARCH ARTICLE

NANO · MICRO small
www.small-journal.com

In Situ Synthesis of Cu_xO/N Doped Graphdiyne with Pyridine N Configuration for Ammonia Production via Nitrate Reduction

Jian Li, Roberto Valenza, and Sophia Haussener**

Electroreduction of nitrate to ammonia provides an interesting pathway for wastewater treatment and valorization. Cu-based catalysts are active for the conversion of NO_3^- to NO_2^- but suffer from an inefficient hydrogenation process of NO_2^-. Herein, Cu_xO/N-doped graphdiyne (Cu_xO/N-GDY) with pyridine N configuration are in situ prepared in one pot. Benefiting from the synergistic effect of pyridinic N in GDY and Cu_xO, the prepared Cu_xO/N-GDY tested in a commercial H-cell achieved a faradaic efficiency of 85% toward NH_3 at -0.5 V versus RHE with a production rate of 340 μmol h^{-1} mg_{cat}^{-1} in 0.1 M KNO_3. When integrating the Cu_xO/N-GDY in an anion exchange membrane flow electrolyzer, a maximum Faradaic efficiency of 89% is achieved at a voltage of 2.3 V and the production rate is 1680 μmol h^{-1} mg_{cat}^{-1} at 3.3 V in 0.1 M KNO_3 at room temperature. Operation at 40 °C further promoted the overall reaction kinetics of NO_3^- to NH_3, but penalized its selectivity with respect to hydrogen evolution reaction. The high selectivity and production rate in this device configuration demonstrate its potential for industrial application.

1. Introduction

Ammonia is an important energy carrier and fertilizer feedstock for many industries and household chemicals.[1] Currently, the large-scale production of ammonia is predominantly achieved by the energy- and capital-intensive Haber–Bosch process, which consumes 1% of the total energy production and results in 1.4% of the global CO_2 emissions.[2] Electrocatalytic ammonia production by using N-containing species has recently attracted great interest owing to the mild conditions and high compatibility with renewable electricity.[3] Compared to N_2 with high dissociation energy (945 kJ mol^{-1}) and low water solubility (Henry's constant 0.62 mM bar^{-1} at 25 °C), nitrate (NO_3^-) is considered an attractive nitrogen precursor for NH_3 electrosynthesis because of its low dissociation energy of the N = O bond (204 kJ mol^{-1}), high water solubility (3.8 M at 25 °C as KNO_3) and wide distribution as pollutant in wastewater.[4]

As the conversion of NO_3^--to-NH_3 involves a complex nine-proton coupled eight-electron transfer and multiple reaction pathways, the precise design of selective catalysts toward NH_3 is challenging. Noble-metal-based catalysts, especially ruthenium oxides/alloys, have shown great promise in nitrate reduction (NO_3RR),[5] but the low abundance and high price severely restrict their large-scale application (Figure S1 and Table S1, Supporting Information). Copper-based materials have recently appeared at the forefront of NO_3RR due to the high abundance, strong adsorption of NO_3^-, and favorable conversion from NO_3^--to-NO_2^-.[6] Nevertheless, the sequential hydrogenation process of NO_2^- under the assistance of Cu is poor due to the weak adsorption of active hydrogen atom (H*),[7] which leads to a low selectivity and activity toward NH_3. Therefore, developing novel Cu-based catalysts that couple the favorable conversion of nitrate to nitrite and the facilitation of subsequent hydrogenation is necessary.

Hybridizing transition metals with heteroatom-doped carbon materials, especially N-doping, has been demonstrated to promote the production of *H and to accelerate the indirect electrochemical hydrogenation reduction process with *H, which thus synergistically promotes the activity and selectivity toward NH_3.[8] Notably, the facilitation of the hydrogenation process closely depends on the configuration of doped N atoms, and the pyridinic N atoms are demonstrated as the most effective ones among pyridinic, pyrrolic, and graphitic N species.[9] However, for widely researched carbon materials (e.g., graphene, carbon nanotube and fullerene), it is difficult to selectively dope a sufficient amount of site-specific pyridinic N. Graphdiyne (GDY), constituted by periodic motifs within the plane framework of sp- and sp^2-carbon atoms, possesses tunable electronic structures, superior electrical conductivity and uniformly expanded pores, which enable kinetically efficient electron/mass transport along in-plane and out-plane directions.[10] Most importantly, the bottom-up synthesis methods of GDYs provide an ideal solution

J. Li, R. Valenza, S. Haussener
Laboratory of Renewable Energy Science and Engineering
Institute of Mechanical Engineering
EPFL
Station 9, Lausanne 1015, Switzerland
E-mail: jian.li@epfl.ch; sophia.haussener@epfl.ch

The ORCID identification number(s) for the author(s) of this article can be found under https://doi.org/10.1002/smll.202310467

DOI: 10.1002/smll.202310467

to achieve sufficient controllable N atom doping via a monomer-design strategy.[11]

H-cells commonly used for characterizing NO_3RR catalysts cannot reproduce the operating conditions of industrially relevant devices due to the mass transport limitation of their design. Flow electrolyzers can instead reach higher current densities through a continuous circulation of reactants. The catalysts for NO_3RR integrated into flow electrolyzers were nevertheless very few (Table S2, Supporting Information), although this device configuration represents the state of the art for water splitting[12] and was intensively investigated for CO_2 reduction[13] and flow batteries.[14]

In this work, we initiated a straightforward and effective approach to prepare Cu_xO/N-GDY catalysts with dominant pyridine-N configuration in one pot. The content of pyridine-N was determined as high as 80%, which was never achieved in previous N-doped carbon materials. Pyridinic N in GDY and Cu_xO synergistically allowed to achieve NH_3 faradaic efficiencies greater than 85% both in a commercial H-cell and an anion exchange membrane (AEM) flow electrolyzer. The effects of nitrate concentration (from 0.001 to 1 M), temperature (25 to 40 °C), and flowfield geometry (single serpentine or interdigitated) on activity and selectivity toward NH_3 were investigated to identify the best operating conditions. At room temperature, the faradaic efficiency and production rate reached 93% and 1950 μmol h^{-1} mg_{cat}^{-1} with a voltage of 3.3 V in 1 M KNO_3, which was the best performance reported in electrolyzer configuration, demonstrating its industrial scale-up potential.

2. Results and Discussion

Cu_xO/N-GDY powder was prepared in one pot by using CuCl, DMF, and pentakis[(trimethylsilyl)ethynyl]pyridine (N-HEB-TMS) as the catalyst, solvent, and monomer, respectively. In brief, N-HEB-TMS and CuCl with a molar ratio of 1:1 were added into a closed reaction bottle containing DMF. After reacting for 24 h (60 °C) in the presence of air, the product precipitated at the bottom of the bottle (**Figure 1a**). The prepared solid was then collected by centrifugation and washed consecutively with DMF, THF, and water. UV-vis absorption and Raman spectroscopy were used to study the chemical structure of the powder. Compared to the UV−visible spectrum of the monomer, a noticeable bathochromic shift was observed in the prepared powder (Figure 1b). Such redshift indicated the enhanced electron delocalization by the extended π-conjugated system, confirming the successful formation of the conjugated diacetylenic linkages.[15] The Raman spectrum showed three prominent bands. The peaks located at 1391.2 and 1568.5 cm^{-1} were assigned to the D band and G band in aromatic rings, respectively. The vibration of the conjugated diyne linkage (–C≡C–) was confirmed at 2179.8 cm^{-1} (Figure 1c). X-ray photoelectron spectroscopy (XPS) and X-ray diffraction (XRD) were further carried out to study the chemical composition, state, and bonds of the prepared powder. The XPS general survey showed that the prepared sample mainly contained elements C, N, O, and Cu (Figure S2, Supporting Information). In detail, the high-resolution spectrum of C 1s can be deconvoluted into five bonds, corresponding to sp^2 (C = C) at 284.5 eV, sp (C≡C) at 285.2 eV, C = O at 288.5 eV, C−O at 287.0 eV, C = N at 286.2 eV, respectively (Figure 1d). For the high-resolution spectrum of N, three subpeaks could be detected, including pyridinic N (399.7 eV), imine N (398.6 eV), and protonated pyridine N (402.0 eV) (Figure 1e). The protonated pyridine N may derive from the pyridinic N interacting with the neighbor carboxyl groups, as the exposed acetylenic groups on the surface will be oxidized in air.[11b] Notably, the ratio of pyridinic N is ≈80%, confirming the dominant configurations of pyridinic N in the sample. The high-resolution XPS spectrum of the Cu 2p showed that the main copper species was Cu^{2+} (934.65 eV), accompanied by a small amount of Cu^+ (932.70 eV) (Figure 1f). A diffraction peak at 22° in the XRD spectra was assigned to the (002) plane of graphite-type carbon (Figure 1g), indicating the distortion from the ordered arrangement of N-GDY along its stacking direction. The peaks located at 38.9° and 61.5° corresponded to the (200) and (−113) crystalline planes of monoclinic CuO (PDF: 80–1917). The amount of Cu was further determined as 9.5% by using inductively coupled plasma mass spectrometry (ICP-MS). All the results above indicated the successful synthesis of Cu_xO/N-GDY with dominant pyridinic N configuration.

The morphology and composition of the as-prepared powder were then characterized by transmission electron microscopy (TEM). A dense distribution of nanoparticles loaded on N-GDY was clearly observed (**Figure 2a**). Electron energy loss spectroscopy (EELS) mapping of the selected region displayed a uniform distribution of Cu, N, O, and C elements, further suggesting the existence of Cu species in the powder (Figure 2b). The high-resolution TEM (HRTEM) micrograph revealed that the nanoparticles exhibited a crystal phase, which can be assigned to the monoclinic phase (space group = C1c1) with a = 4.6893 Å b = 3.4268 Å and c = 5.1321 Å. The lattice fringe distances were measured to be 0.253, 0.236, and 0.239 nm, corresponding to (11-1), (111), and (002) planes of monoclinic CuO (Figure 2c).

Electrochemical nitrate reduction of Cu_xO/N-GDY was first tested in a commercial H-cell under ambient conditions in 0.1 M KOH solution containing 0.1 M KNO_3. The Cu_xO/N-GDY was deposited onto a carbon paper electrode with a fixed catalyst mass loading of 0.4 mg cm^{-2}. The linear sweep voltammetry (LSV) with and without KNO_3 was performed to study the activity of Cu_xO/N-GDY toward NO_3RR. Compared to the electrolyte without NO_3^-, the enhanced current density indicated the effective reduction of NO_3^- by the Cu_xO/N-GDY (**Figure 3a**). The selectivity of products was further confirmed by holding a certain potential each time for 0.5 h, in which the produced NH_3 products were quantified by UV–Vis spectroscopy (Figure S3, Supporting Information). As shown in Figure 3b, the Cu_xO/N-GDY displayed an improved selectivity with the decreased potential and reached an optimal faradaic efficiency of 85% at −0.5 V versus RHE with a production rate of 340 μmol h^{-1} mg_{cat}^{-1}. A further decrease in the potential slightly reduced the selectivity toward NH_3 due to the enhanced H_2 selectivity.[6a,16] Unlike the faradic efficiency, the production rate and partial current density of NH_3 gradually increased when applying a more negative potential, generating a production rate of 620 μmol h^{-1} mg_{cat}^{-1} at −0.7 V versus RHE despite a reduction of faradaic efficiency to 77% (Figure 3d). As a comparison, the bare carbon paper electrode, N-GDY/carbon paper electrode, and Cu_xO/GDY/carbon paper electrode were prepared and tested under the same conditions (Figure 3c,d). The bare carbon paper electrode without Cu_xO/N-GDY showed negligible activity and selectivity toward NH_3. In the absence of

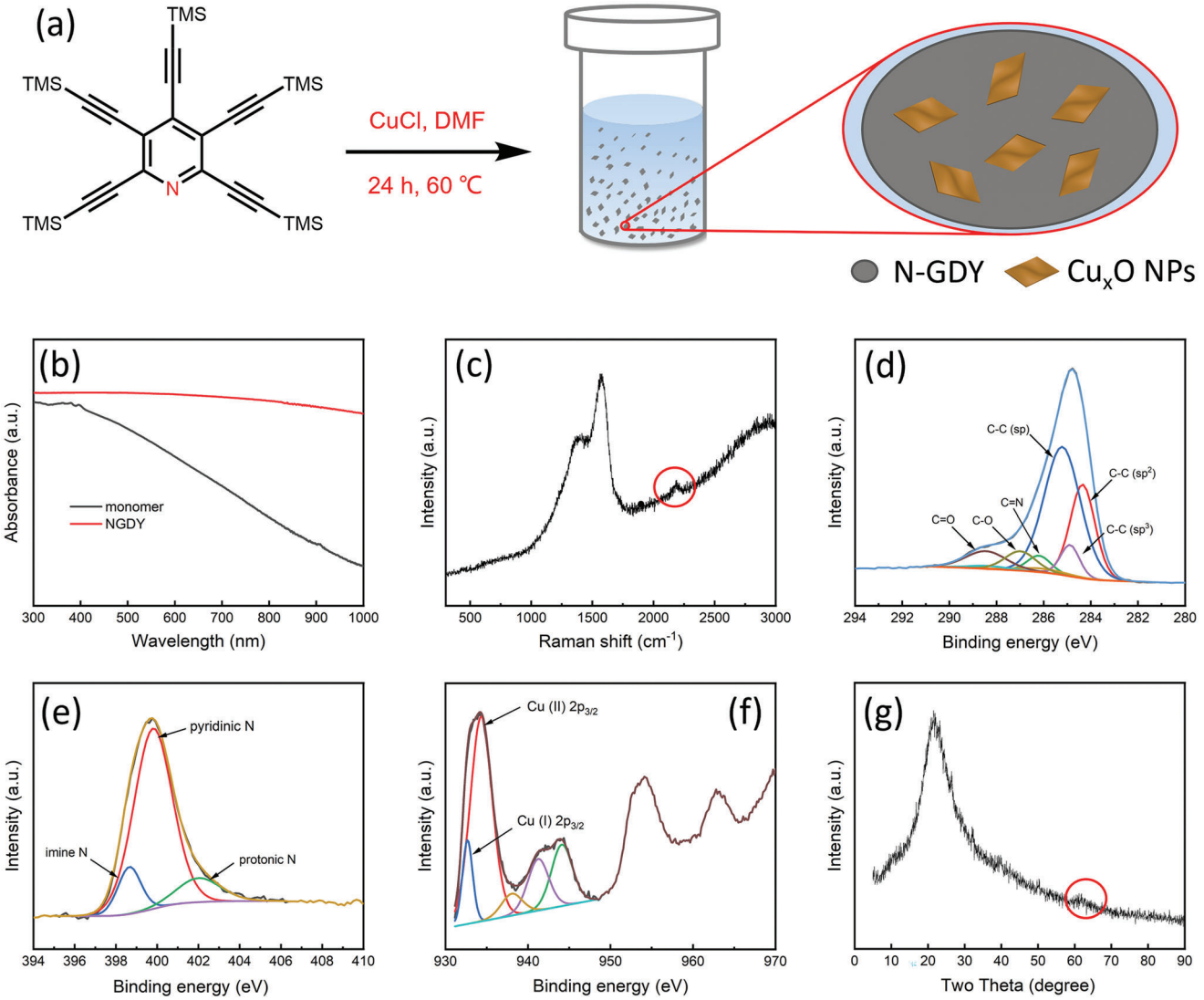

Figure 1. In situ preparation of Cu_xO/N-GDY in one pot and the characterizations. a) Simplified schematic diagram of synthesis of Cu_xO/N-GDY with pyridine N configuration; b) UV–Vis spectrum of monomer and N-GDY; c) Raman spectrum of N-GDY; d) high-resolution C 1s spectrum; e) high-resolution N 1s spectrum and f) high-resolution Cu 2p spectrum of Cu_xO/N-GDY; g) XRD spectrum of Cu_xO/N-GDY.

either Cu_xO or N, both the selectivity and activity toward NH_3 decreased remarkably. These results indicated that the synergistic effect between pyridinic N in GDY and Cu_xO played a crucial role in achieving a high selectivity and activity toward NH_3, which was further confirmed by the reduction of the charge transfer resistance in the electrochemical impedance spectroscopy (EIS) (Figure S4, Supporting Information). In addition, a direct comparison with a commercial Cu foil was carried out. Compared to commercial Cu foil, the Cu_xO/NGDY exhibited much higher selectivity and production rate toward NH_3 over a wide potential range (Figure S5, Supporting Information), further confirming the high selectivity and activity of Cu_xO/NGDY toward NH_3.

The main byproduct of nitrate reduction of Cu_xO/N-GDY was NO_2^-, as detected and quantified by UV–Vis spectroscopy (Figure S6, Supporting Information). The FE of NO_2^- was determined as 30% at −0.3 V versus RHE, followed by a gradual decrease to a minimum of 4% at −0.7 V versus RHE (Figure 3b). Such a trend is associated with the increased selectivity toward NH_3, confirming that NO_2^- is an intermediate product that can be further reduced to NH_3 under more negative potential. H_2 as another side product was further confirmed by gas chromatography. To confirm that the produced NH_3 was derived from NO_3^- ions, ^1H NMR experiment was performed by using ^{15}N-labeled NO_3^- as a reactant. Only two peaks corresponding to $^{15}NH_4^+$ were clearly observed after 0.5 h of electrolysis under −0.5 V versus RHE (Figure 3e).

When increasing the experiment duration, the peak intensity of $^{15}NH_4^+$ was enhanced and no other peaks appeared, indicating that the generated NH_3 came from the reduction of nitrate instead of the N in N-GDY or contaminants. Based on the NMR peak areas ratio between $^{15}NH_4^+$ and maleic acid in electrolysis tests and the calibration curve of $^{15}NH_4^+$ (Figure S7, Supporting Information), the FE of NH_3 was determined as 83%, consistent with the results of UV–Vis spectroscopy. In addition, the

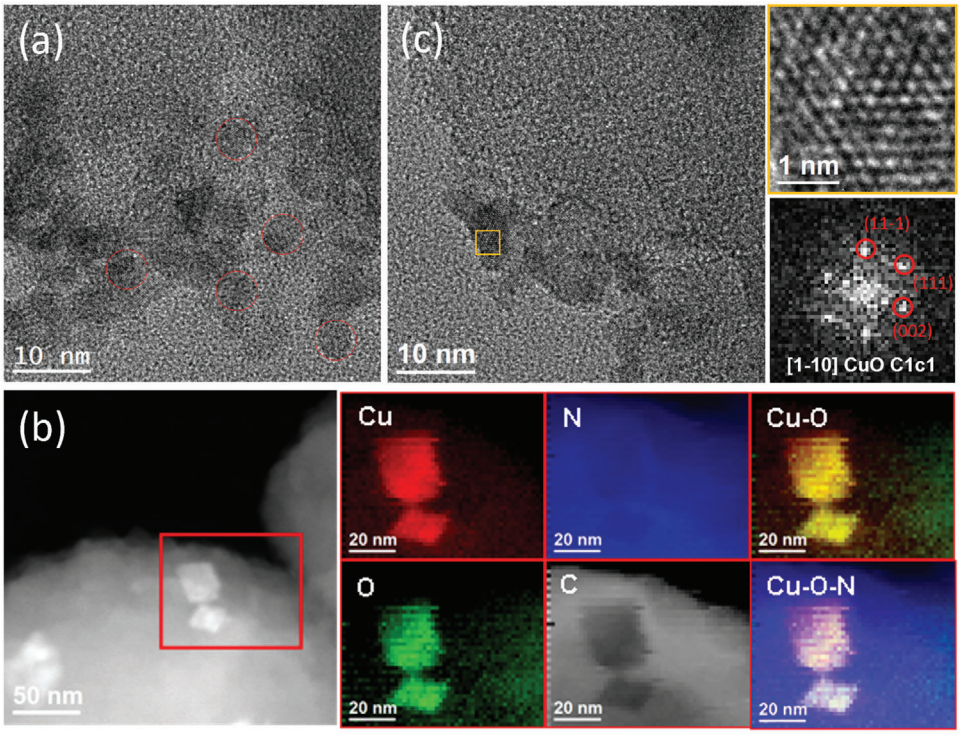

Figure 2. TEM of the as-prepared Cu_xO/N-GDY. a) HAADF STEM image and b) the corresponding EELS mapping of the selected red-squared region of Cu_xO/N-GDY; c) HRTEM image of CuO in N-GDY, magnification of the yellow-squared region, and its corresponding indexed power spectrum (FFT).

performance of Cu_xO/N-GDY with different NO_3^- concentrations ranging from 0.001 to 1.0 M was further evaluated (Figure 3f). The FEs and production rate of NH_3 greatly decreased when reducing the concentration to 0.01 or 0.001 M. For 1.0 M NO_3^-, the maximum of NH_3 faradaic efficiency shifted to more negative potentials, reaching 87% at −0.7 versus RHE.

To detect the intermediates and monitor the mechanism, in situ ATR-FTIR spectra were carried out. The ATR-FTIR spectrum was recorded in 1 M KOH solution containing 0.1 M KNO_3 and the signal was collected from 1000 to 4000 cm^{-1}. As shown in Figure S8, the peaks observed were assigned to different nitrogen intermediates. The peak located at 1290 cm^{-1} corresponded to the $*NO_2^-$ stretching mode,[17] indicating the presence of deoxygenation steps during NO_3^- reduction. Additionally, the σ (N−H) bending mode of NH_x species was observed at 1650 cm^{-1};[17] the characteristic peaks of $*NH_2$ were detected at 3210 and 1150 cm^{-1};[5a] and the peak at 1460 cm^{-1} was attributed to the characteristic frequency of $*NH_4^+$.[18] The results demonstrated that the deoxygenation step was followed by a sequence of protonation processes for ammonia production.

Cu_xO/N-GDY was then integrated into an anion-exchange membrane electrolyzer to test industrially relevant operating conditions (Figures S9 and S10, Supporting Information). The FEs of NH_3 displayed a similar trend to the one in the H-cell and reached a maximum of 89% at 2.3 V in 0.1 M KNO_3 (**Figure 4a**). With an energy efficiency of 21% (Equation S5, Supporting Information), a NH_3 production rate of 585 μmol h^{-1} mg_{cat}^{-1} was achieved, almost 1.7 times higher than the one obtained at the maximum FE point in H-cell. The additional convective flux of NO_3^- in the electrolyzer mitigated the mass transfer limitation characteristic of the H-cell design. When reducing the concentration of KNO_3 to 0.01 M or to 0.001 M, both the FE and production rate of NH_3 decreased due to the smaller flux of NO_3^- reaching the surface of the catalysts (Figure 4b). In the 1 M KNO_3 solution, NO_3^- conversion appears to be limited by the kinetics of the electrochemical reaction. The FEs and production rates of NH_3 were lower for voltages below 2.7 V due to the kinetically more favorable reduction of NO_3^- to NO_2^- (Figure 4c). For the NO_3^- concentrations in which mass transport is not the limiting factor, the reduction of NO_3^- to NO_2^- is the rate-determining step at low voltages. This is observable from the accumulation of NO_2^- (Figure 4d), consistent with previous reports.[19] When applying a voltage greater than 2.7 V, the FE and production rate of NH_3 in 1 M KNO_3 increased reaching a maximum FE of 93% and a production rate of 1950 μmol h^{-1} mg_{cat}^{-1} at 3.3 V, the highest value reported in this device configuration (Figures S11 and Table S2, Supporting Information). The effects of the variation in NO_3^- concentration are detailed in Section S3. The stability of the AEM device was further tested at a voltage of 2.3 V. As shown in Figure 4e, the device was relatively stable, and only a 15% decline of current was observed after 20 h test. The decrease possibly resulted from the detachment of the carbon particles in the pores of the fibers of the porous layer on which Cu_xO/N-GDY was deposited, as evidenced by the SEM images after electrolysis (Figure S12, Supporting Information). Notably, the FEs of NH_3 maintained almost the same during the 20 h test, further confirming the stability of Cu_xO/N-GDY catalyst (Figure S13, Supporting Information).

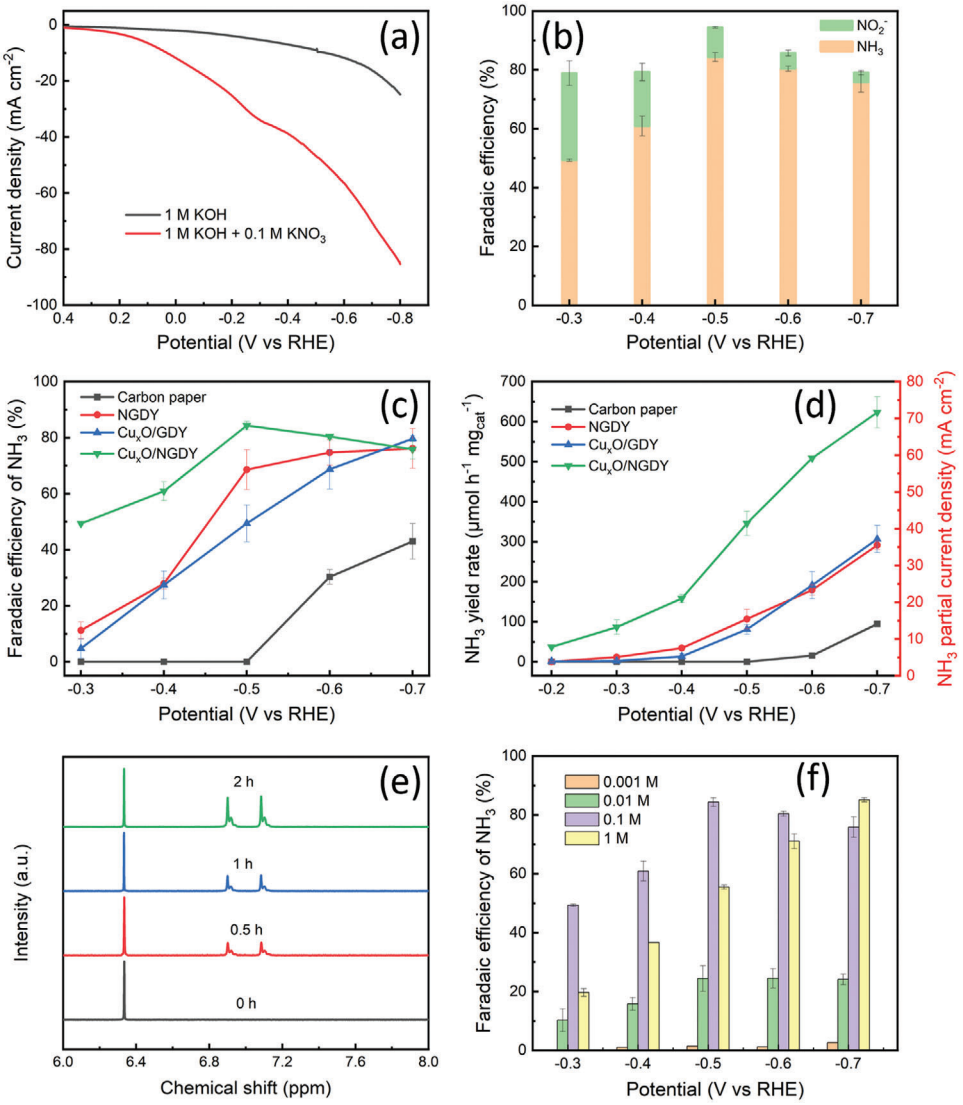

Figure 3. The electrochemical characterization of the as-prepared Cu_xO/N-GDY in a H cell. a) LSV curves of Cu_xO/N-GDY in 1 M KOH electrolyte and 0.1 M KNO_3/1 M KOH mixed electrolyte; b) faradaic efficiency of NH_3 and NO_2^- at different potential; c) faradaic efficiency of NH_3 of Cu_xO/N-GDY, N-GDY, Cu_xO/GDY and bare carbon paper; d) the production rate of NH_3 of Cu_xO/N-GDY, N-GDY, Cu_xO/GDY and bare carbon paper at different potential; e) ^1H NMR spectra for electrolytes after $^{15}NO_3^-$ reduction tests of different duration; f) faradaic efficiency of NH_3 in different concentrations of KNO_3 at different potential.

To determine the effect of temperature on NH_3 selectivity and activity of the Cu_xO/N-GDY, the AEM electrolyzer was further tested at 40 °C. The peak of ammonia faradaic efficiency shifted to a lower voltage mainly due to the reduction of the standard equilibrium voltage of NO_3RR coupled with oxygen evolution reaction and of kinetic and ohmic losses at a fixed current density (Figure 4f). The NH_3 production rate is enhanced especially at high voltages by the expected better NO_3RR kinetics but it is partially penalized by the worse selectivity with respect to HER (Figure 4g). A more detailed analysis of the effects of temperature on the system is reported in Section S4.

A comparison between an interdigitated flowfield geometry and the previously used single serpentine flowfield was then performed (Figure S14, Supporting Information). The effect of a different NO_3^- and NO_2^- distribution in the catalyst-coated porous substrate on the activity and NH_3 selectivity was investigated in a 0.1 M NO_3^- solution. The selectivity and activity of Cu_xO/N-GDY catalyst reported in Figure 4h,i was not strongly impacted by the variation of flowfield configuration, confirming the kinetic limitation of NH_3 production rate at low voltages. At voltages larger than 2.7 V, the interdigitated flow field showed a slightly better production rate. The forced flux of NO_3^- under the rib in the interdigitated geometry might be beneficial for the partial mitigation of the mass transport limitation. Optimization of the flowfield pattern coupling computational fluid dynamics calculations with a larger number of tests varying NO_3^- concentration and flow rate as proposed for other technologies[20] represent a possible future activity to further optimize devices for the electroreduction of nitrate to ammonia.

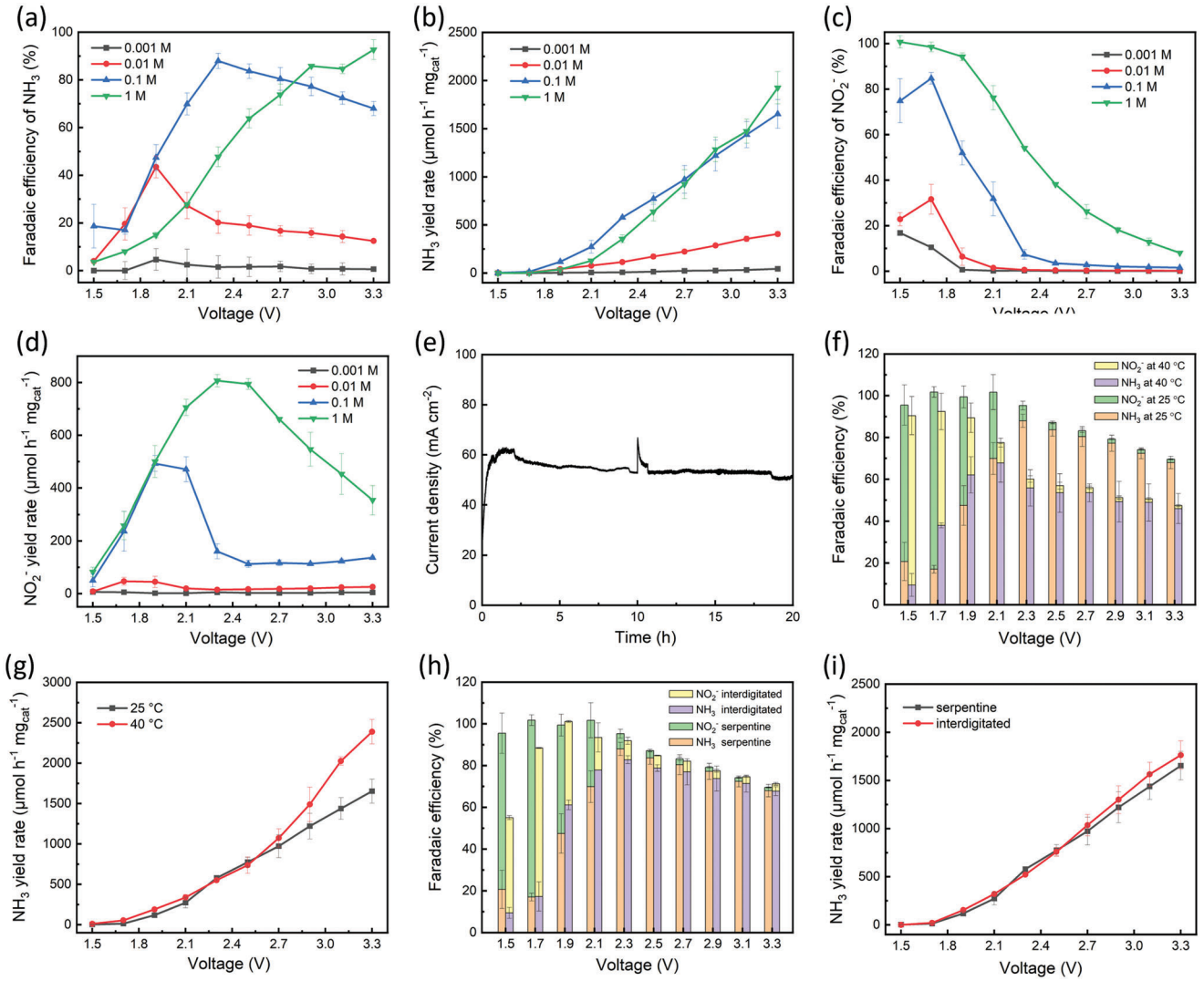

Figure 4. The electrochemical characterization of the as-prepared Cu_xO/N-GDY in an anion exchange membrane flow electrolyzer. a) Faradaic efficiency of NH_3 in different concentrations of KNO_3; b) the production rate of NH_3 in different concentrations of KNO_3; c) faradaic efficiency of NO_2^- in different concentrations of KNO_3; d) the production rate of NO_2^- in different concentration of KNO_3; e) the stability test of Cu_xO/N-GDY in 0.1 M KNO_3 with a voltage of 2.3 V; f) faradaic efficiency of NH_3 and NO_2^- at different temperature; g) the production rate of NH_3 at different temperature; h) faradaic efficiency of NH_3 and NO_2^- in different flow channels; i) the production rate of NH_3 in different flow channels.

3. Conclusion

In conclusion, Cu_xO/N-GDY with pyridine N configuration was in situ prepared in one pot. Benefiting from the synergistic effect of pyridinic N in GDY and Cu_xO, the catalyst tested in 0.1 M KNO_3 exhibited a maximum faradaic efficiency toward NH_3 of 85.0% and a production rate of 340 μmol h^{-1} mg_{cat}^{-1} at −0.5 V versus RHE in a commercial H-cell. When integrating the Cu_xO/N-GDY in an AEM electrolyzer, a maximum faradaic efficiency of 89% with a voltage of 2.3 V and a production rate of 1950 μmol h^{-1} mg_{cat}^{-1} at 3.3 V were obtained, the best performance reported in this device configuration. Operation at higher temperatures improved the overall reaction kinetics of NO_3^- reduction but lowered the maximum faradaic efficiency toward NH_3. This work provides a straightforward method for the synthesis of hybrid catalysts on the basis of pyridine N-doped carbon materials, paving the way for new designs of cheap and efficient NO_3RR catalysts. The integration of Cu_xO/N-GDY in an AEM electrolyzer is a first step toward the industrial scale-up of the technology, which can be further developed by directly depositing the catalysts and ionomers on the membrane to avoid the use of the supporting electrolyte, or studying the mass-transport limited regime of the system for applications in which the cogeneration of H_2 and NH_3 at maximal production rates is preferred to selectivity.

Supporting Information

Supporting Information is available from the Wiley Online Library or from the author.

Acknowledgements

J.L. and S.H. acknowledge funding from the European Union's Horizon 2020 research and innovation program under the Marie Sklodovska-Curie Grant Agreement No 101030637. R.V. and S.H. acknowledge funding from the European Union's Horizon 2020 research and innovation program under the Marie Sklodovska-Curie Grant Agreement No 861151.

Open access funding provided by Ecole Polytechnique Federale de Lausanne.

Conflict of Interest

The authors declare no conflict of interest.

Data Availability Statement

The data that support the findings of this study are available from the corresponding author upon reasonable request.

Keywords

ammonia production, electrocatalysis, graphdiyne, N doping, nitrate reduction

Received: February 2, 2024
Revised: March 18, 2024
Published online:

[1] V. Rosca, M. Duca, M. T. de Groot, M. T. M. Koper, *Chem. Rev.* **2009**, *109*, 2209.
[2] M. Capdevila-Cortada, *Nat. Catal.* **2019**, *2*, 1055.
[3] a) G. Qing, R. Ghazfar, S. T. Jackowski, F. Habibzadeh, M. M. Ashtiani, C.-P. Chen, M. R. Smith III, T. W. Hamann, *Chem. Rev.* **2020**, *120*, 5437; b) S. C. D'Angelo, A. J. Martín, S. Cobo, D. F. Ordóñez, G. Guillén-Gosálbez, J. Pérez-Ramírez, *Energy Environ. Sci.* **2023**, *16*, 3314; c) Z. Ren, K. Shi, X. Feng, *ACS Energy Lett.* **2023**, *8*, 3658.
[4] a) J.-X. Liu, D. Richards, N. Singh, B. R. Goldsmith, *ACS Catal.* **2019**, *9*, 7052; b) Z.-Y. Wu, M. Karamad, X. Yong, Q. Huang, D. A. Cullen, P. Zhu, C. Xia, Q. Xiao, M. Shakouri, F.-Y. Chen, J. Y. Kim, Y. Xia, K. Heck, Y. Hu, M. S. Wong, Q. Li, I. Gates, S. Siahrostami, H. Wang, *Nat. Commun.* **2021**, 12.
[5] a) S. Han, H. Li, T. Li, F. Chen, R. Yang, Y. Yu, B. Zhang, *Nat. Catal.* **2023**, *6*, 402; b) J. Li, G. Zhan, J. Yang, F. Quan, C. Mao, Y. Liu, B. Wang, F. Lei, L. Li, A. W. M. Chan, L. Xu, Y. Shi, Y. Du, W. Hao, P. K. Wong, J. Wang, S.-X. Dou, L. Zhang, J. C. Yu, *J. Am. Chem. Soc.* **2020**, *142*, 7036; c) F.-Y. Chen, Z.-Y. Wu, S. Gupta, D. J. Rivera, S. V. Lambeets, S. Pecaut, J. Y. T. Kim, P. Zhu, Y. Z. Finfrock, D. M. Meira, G. King, G. Gao, W. Xu, D. A. Cullen, H. Zhou, Y. Han, D. E. Perea, C. L. Muhich, H. Wang, *Nat. Nanotechnol.* **2022**, *17*, 759; d) Y. Yao, L. Zhao, J. Dai, J. Wang, C. Fang, G. Zhan, Q. Zheng, W. Hou, L. Zhang, *Angew. Chem., Int. Ed.* **2022**, *61*, 202208215.
[6] a) J.-Y. Fang, Q.-Z. Zheng, Y.-Y. Lou, K.-M. Zhao, S.-N. Hu, G. Li, O. Akdim, X.-Y. Huang, S.-G. Sun, *Nat. Commun.* **2022**, *13*, 7899; b) Q. Hu, Y. Qin, X. Wang, Z. Wang, X. Huang, H. Zheng, K. Gao, H. Yang, P. Zhang, M. Shao, C. He, *Energy Environ. Sci.* **2021**, *14*, 4989; c) Q. Hu, Y. Qin, X. Wang, H. Zheng, K. Gao, H. Yang, P. Zhang, M. Shao, C. He, *CCS Chem.* **2022**, *4*, 2053; d) Y. Fu, S. Wang, Y. Wang, P. Wei, J. Shao, T. Liu, G. Wang, X. Bao, *Angew. Chem., Int. Ed.* **2023**, *62*, 202303327; e) Y. Wang, W. Zhou, R. Jia, Y. Yu, B. Zhang, *Angew. Chem., Int. Ed.* **2020**, *59*, 5350.
[7] a) W. He, J. Zhang, S. Dieckhöfer, S. Varhade, A. C. Brix, A. Lielpetere, S. Seisel, J. R. C. Junqueira, W. Schuhmann, *Nat. Commun.* **2022**, *13*, 1129; b) H. Liu, X. Lang, C. Zhu, J. Timoshenko, M. Rüscher, L. Bai, N. Guijarro, H. Yin, Y. Peng, J. Li, Z. Liu, W. Wang, B. R. Cuenya, J. Luo, *Angew. Chem., Int. Ed.* **2022**, *61*, 202202556; c) X. Zhao, K. Zhao, X. Quan, S. Chen, H. Yu, Z. Zhang, J. Niu, S. Zhang, *Chem. Eng. J.* **2021**, *415*, 128958.
[8] a) R. Li, T. Gao, W. Qiu, M. Xie, Z. Jin, P. Li, *Nano Res.* **2024**, *17*, 2438; b) Y. Lan, J. Chen, H. Zhang, W. Zhang, J. Yang, *J. Mater. Chem. A* **2020**, *8*, 15853; c) X. Zhang, G. Ma, L. Shui, G. Zhou, X. Wang, *Chem. Eng. J.* **2022**, *430*, 132666.
[9] a) J. Zhao, B. Shang, J. Zhai, *Nanomaterials* **2021**, *11*, 2418; b) Y. Liu, Y. Su, X. Quan, X. Fan, S. Chen, H. Yu, H. Zhao, Y. Zhang, J. Zhao, *ACS Catal.* **2018**, *8*, 1186; c) S. Zhang, M. Li, J. Li, Q. Song, X. Liu, *Proc. Natl. Acad. Sci. U.S.A.* **2023**, *120*, 2207080119.
[10] a) J. Li, X. Gao, L. Zhu, M. N. Ghazzal, J. Zhang, C.-H. Tung, L.-Z. Wu, *Energy Environ. Sci.* **2020**; b) F. He, Y. Li, *CCS Chem.* **2023**, *5*, 72; c) Y. Fang, Y. Liu, L. Qi, Y. Xue, Y. Li, *Chem. Soc. Rev.* **2022**, *51*, 2681; d) X. Zheng, S. Chen, J. Li, H. Wu, C. Zhang, D. Zhang, X. Chen, Y. Gao, F. He, L. Hui, H. Liu, T. Jiu, N. Wang, G. Li, J. Xu, Y. Xue, C. Huang, C. Chen, Y. Guo, T.-B. Lu, D. Wang, L. Mao, J. Zhang, Y. Zhang, L. Chi, W. Guo, X.-H. Bu, H. Zhang, L. Dai, Y. Zhao, et al., *ACS Nano* **2023**, *17*, 14309.
[11] a) J. Li, L. Zhu, C.-H. Tung, L.-Z. Wu, *Angew. Chem., Int. Ed.* **2023**, *62*, 202301384; b) H. Shang, Z. Zuo, H. Zheng, K. Li, Z. Tu, Y. Yi, H. Liu, Y. Li, Y. Li, *Nano Energy* **2018**, *44*, 144; c) G. Li, Y. Li, H. Liu, Y. Guo, Y. Li, D. Zhu, *Chem. Commun.* **2010**, *46*, 3256; d) J. Li, X. Han, D. Wang, L. Zhu, M.-H. Ha-Thi, T. Pino, J. Arbiol, L.-Z. Wu, M. Nawfal Ghazzal, *Angew. Chem., Int. Ed.* **2022**, *61*, 202210242.
[12] a) M. Carmo, D. L. Fritz, J. Mergel, D. Stolten, *Int. J. Hydrogen Energy* **2013**, *38*, 4901; b) I. Vincent, D. Bessarabov, *Renew. Sustain. Energy Rev.* **2018**, *81*, 1690; c) K. Zeng, D. Zhang, *Prog. Energy Combust. Sci.* **2010**, *36*, 307.
[13] a) D. Wu, F. Jiao, Q. Lu, *ACS Catal.* **2022**, *12*, 12993; b) B. Endrődi, G. Bencsik, F. Darvas, R. Jones, K. Rajeshwar, C. Janáky, *Prog. Energy Combust. Sci.* **2017**, *62*, 133.
[14] X. Ke, J. M. Prahl, J. I. D. Alexander, J. S. Wainright, T. A. Zawodzinski, R. F. Savinell, *Chem. Soc. Rev.* **2018**, *47*, 8721.
[15] J. Zhou, X. Gao, R. Liu, Z. Xie, J. Yang, S. Zhang, G. Zhang, H. Liu, Y. Li, J. Zhang, Z. Liu, *J. Am. Chem. Soc.* **2015**, *137*, 7596.
[16] Q. Gao, B. Yao, H. S. Pillai, W. Zang, X. Han, Y. Liu, S.-W. Yu, Z. Yan, B. Min, S. Zhang, H. Zhou, L. Ma, H. Xin, Q. He, H. Zhu, *Nat. Synth.* **2023**, *2*, 624.
[17] N. Zhang, J. Shang, X. Deng, L. Cai, R. Long, Y. Xiong, Y. Chai, *ACS Nano* **2022**, *16*, 4795.
[18] Z. Song, Y. Liu, Y. Zhong, Q. Guo, J. Zeng, Z. Geng, *Adv. Mater.* **2022**, *34*, 2204306.
[19] a) M. Duca, M. T. M. Koper, *Energy Environ. Sci.* **2012**, *5*, 9726; b) M. T. de Groot, M. T. M. Koper, *J. Electroanal. Chem.* **2004**, *562*, 81.
[20] a) M. Messaggi, P. Canzi, R. Mereu, A. Baricci, F. Inzoli, A. Casalegno, M. Zago, *Appl. Energy* **2018**, *228*, 1057; b) M. Filippi, T. Möller, L. Liang, P. Strasser, *Energy Environ. Sci.* **2023**, *16*, 5265; c) B. Jung, S. Park, C. Lim, W. H. Lee, Y. Lim, J. Na, C.-J. Lee, H.-S. Oh, U. Lee, *Chem. Eng. J.* **2021**, *424*, 130265.